THE UNIVERSITY *of* EDINBURGH

# Edinburgh Research Explorer

# Phase behaviour of the quantum Lennard-Jones solid

OPEN ACCESS

# Phase behaviour of the quantum Lennard-Jones solid

H. Wiebe,[1, a)] T. L. Underwood,[2] and G. J. Ackland[1]

[1)] *School of Physics & Astronomy, The University of Edinburgh, Edinburgh,*
*EH9 3JZ, United Kingdom.*

[2)] *Department of Chemistry, University of Bath, Bath, BA2 7AY,*
*United Kingdom.*

The Lennard-Jones potential is perhaps one of the most widely-used models for the interaction of uncharged particles, such as noble gas solids. The phase diagram of the classical LJ solid is known to exhibit transitions between hcp and fcc phases. However, the phase behaviour of the quantum Lennard-Jones solid remains unknown. Thermodynamic integration based on path integral molecular dynamics and lattice dynamics calculations are used to study the phase stability of the hcp and fcc Lennard-Jones solids. The hcp phase is shown to be stabilized by quantum effects in PIMD while fcc is shown to be favoured by lattice dynamics, which suggests a possible re-entrant low pressure fcc phase for highly quantum systems. Implications for the phase stability of noble gas solids are discussed. For parameters equating to Helium, the expansion due to zero-point vibrations is associated with quantum melting: neither crystal structure is stable at zero pressure.

---
[a)]Electronic mail: h.wiebe@ed.ac.uk

## I. INTRODUCTION

Since its inception in 1924, the Lennard-Jones (LJ) potential,[1]

$$U_{\text{LJ}}(r) = 4\varepsilon \left[ \left( \frac{\sigma}{r} \right)^{12} - \left( \frac{\sigma}{r} \right)^{6} \right],  \tag{1}$$

has remained the canonical model for short-ranged particle interactions. The properties of this potential are uniquely defined due to the presence of only two parameters, $\sigma$ and $\varepsilon$, which set the length and energy scales respectively. Despite this simplicity, the LJ system shows remarkably rich phase behavior, including transitions between hexagonal close packed (hcp) and face-centered cubic (fcc) solids.[2–7] For the classical system hcp is the most stable phase at low temperature and pressure conditions, with fcc becoming preferred upon heating and/or compression. However, the free energy differences between hcp and fcc are small, and careful calculation of long-range interactions as well as both harmonic and anharmonic thermal effects are important.[8,9]

The attractive $1/r^6$ part of the potential describes van der Waals interactions, making it suitable for studying the noble gas elements. Indeed, at low pressures the heavy noble gas elements such as Ar, Xe and Kr[10,11], as well as small molecules like methane,[12] are well described as classical particles interacting via the LJ potential. However, as the density of the system is increased or the mass of the particles is decreased, quantum effects become increasingly important. He, the lightest of the noble gas elements, is dominated by quantum effects. This has motivated investigations into the *quantum* LJ system, which is far more complicated than the classical system. For one thing the uniqueness of the phase diagram is lost: in the quantum system there is an additional free parameter, $\hbar^2/2m$, which corresponds to the "quantumness" of the particles.[13]

The solid phase of the quantum LJ system has been investigated using a number of computational methods.[13–23] These include quasi-harmonic lattice dynamics (QHLD), classical molecular dynamics, and path-integral methods. QHLD[24] captures effects such as the zero-point energy which are inaccessible to classical methods. However, it cannot capture anharmonic effects associated with interacting phonons, something well known to play an important role in quantum crystals[21,25,26]. Path integral methods[27,28] do not suffer from this shortcoming, capable in principle of providing exact properties of quantum systems. These methods exploit the path integral formulation of quantum mechanics, and sample the configuration space of the quantum system using molecular dynamics (PIMD) or Monte Carlo.

However, the downside of these methods is that they are more computationally demanding than QHLD.

The focus of previous studies has been on properties such as the thermal expansion and heat capacity of the quantum LJ solid. These studies all assumed fcc to be the stable solid phase. However, as mentioned above, the classical LJ solid exhibits regions of both fcc *and* hcp stability, and thus the expectation is that the phase diagram of the quantum LJ solid should also exhibit both these phases. Interestingly, an exploration of the solid phase diagram in this system has not yet been undertaken. Experimentally, while there is some uncertainty with regards to the question of hcp vs. fcc stability in Ne, Ar, Kr and Xe at low pressures, it appears that the fcc phase is at least metastable in these systems.[29] By contrast, He is exceptional in that hcp is the observed phase (notwithstanding a small region of bcc stability near melting at low pressures).[26] It is not known why He readily takes the hcp structure. One might speculate that quantum effects somehow act to stabilise the hcp structure, and that the effect is more pronounced in He than the heavier noble gas elements due to its high quantumness. An investigation into the phase behaviour of the quantum LJ solid will shine light on this.

Here, we use PIMD in combination with QHLD to determine the phase diagram of the quantum LJ solid, focusing on low pressure regime. We determine the relative stability of hcp and fcc for a range of quantumnesses, ranging from the classical limit to that comparable to He. In Section II we describe our model for the LJ solid, including approximations utilised in our calculations. Full descriptions of the PIMD and QHLD methodologies employed are provided in the supplementary materials. Results of our PIMD calculations are presented in Section III, followed by results of our QHLD calculations in Section IV. In Section V we reconcile the PIMD and QHLD results and discuss their implications for the noble gas elements. Finally, in Section VI we restate our main conclusions.

## II.    MODEL

We consider a system of $N$ *distinguishable* quantum particles interacting via the LJ potential (Eqn. 1). We emphasise that we do not consider exchange effects, which in the LJ solid are expected to be insignificant for the range of quantumnesses we consider.[13,30] Further justification for this assumption is provided in the supplementary material.    In

addition, the systems we consider are perfect crystals without point defects such as vacancies or interstitials. Defects have been shown to be important for the observation of supersolid behaviour in quantum systems,[31] but would not affect the relative stability of hcp and fcc phases and are therefore not included here.

## A. Reduced units

As the length and energy scales are set by the $\sigma$ and $\varepsilon$ parameters, it is convenient to define all physical properties of the system in terms of dimensionless reduced units, as in Table I. The inclusion of quantum effects adds a second lengthscale to the system: the

TABLE I. Reduced units defined in terms of model parameters $\sigma$ and $\varepsilon$.

| Quantity | Expression |
| --- | --- |
| Length | $r^* = r/\sigma$ |
| Energy | $E^* = E/\varepsilon$ |
| Free energy | $F^* = F/\varepsilon$ |
| Temperature | $T^* = k_B T/\varepsilon$ |
| Density | $\rho^* = \rho\sigma^3$ |
| Pressure | $P^* = P\sigma^3/\varepsilon$ |
| Time | $t^* = t\sqrt{\varepsilon/(m\sigma^2)}$ |
| Quantumness | $\Lambda^* = \hbar/(\sigma\sqrt{m\varepsilon})$ |

de Boer parameter[32] $\Lambda^*$. This is a dimensionless quantity which describes the relationship between the particle diameter $\sigma$ and the de Broglie wavelength of particles with energy $\varepsilon$. Large values of $\Lambda^*$ indicate a more delocalized quantum system, while $\Lambda^* = 0$ corresponds to the classical limit. In this unit system, the mass of the particle $m$ is a dimensionless parameter uniquely defined by the value of $\Lambda^*$, $\sigma$ and $\epsilon$. For the noble gases $\Lambda^*$ ranges from $\approx 0.01$ (for Xe) to $\approx 0.4$ (for He).[26] Thus we consider the range $\Lambda^* = 0$ to $0.4$ in this work.

4

## B.  Truncation scheme

In MD simulations it is necessary to truncate the potential interactions in order to avoid artefacts due to self-interaction through the periodic boundary. Previous work[3,8,9] has demonstrated that for the classical LJ solid one must take great care with regards to the truncation scheme and the treatment of the long-range interactions. The most commonly-used scheme is to shift the potential so that it is continuous at some cutoff radius $r_c^*$:

$$U_{\mathrm{STS}}(r^*) = \begin{cases} U_{\mathrm{LJ}}(r^*) - U_{\mathrm{LJ}}(r_c^*) & \text{if } r^* < r_c^* \\ 0 & \text{if } r^* > r_c^*. \end{cases} \tag{2}$$

This treatment, referred to as the spherically truncated and shifted (STS) model, avoids errors from discontinuous jumps in the potential but it fails to account for the interactions occurring beyond $r_c^*$. It therefore displays differing phase behaviour from the "true" LJ potential.[3] Conventional tail corrections,[33] which assume that the radial distribution function $g(r^*)$ is uniform and equal to 1 at $r^* > r_c^*$, are not useful for our purposes because they are independent of the crystal structure.

Instead, the contributions of these long-range interactions to the total energy of the system can be accounted for using what we will refer to here as the ground state perturbation (GSP) model.[3] Here the ground state of the LJ system, where all particles reside on their lattice sites, is treated exactly and only the excitations of the system are subject to truncation. To do so, we introduce a correction term to the potential:

$$U_{\mathrm{GSP}}(r^*) = U_{\mathrm{STS}}(r^*) + U_{\mathrm{LRC}}, \tag{3}$$

where $U_{\mathrm{LRC}}$ is defined by

$$U_{\mathrm{LRC}} = U_{\mathrm{GS}}(\rho^*) - \frac{1}{2} \sum_{i,j:R_{ij}<r_c} U_{\mathrm{STS}}(R_{ij}), \tag{4}$$

$U_{\mathrm{GS}}(\rho^*)$ is the ground state energy of the untruncated "true" LJ system at density $\rho^*$ and $R_{ij}$ is the inter-particle distance in said ground state. The $U_{\mathrm{GS}}(\rho^*)$ term is found from lattice-summation[2,34–36] as

$$U_{\mathrm{GS}}(\rho^*) = 2\left[\left(\frac{\rho^*}{\sqrt{2}}\right)^4 A_{12} - \left(\frac{\rho^*}{\sqrt{2}}\right)^2 A_6\right]. \tag{5}$$

The $A_{12}$ and $A_6$ terms have been tabulated for different phases of the LJ solid, and in this work parameters for the fcc and hcp phases were taken from ref. 37. For simulations in

5

the $NVT$ ensemble where density is constant, the $U_{\text{LRC}}$ term simply amounts to a constant shift in the relative fcc and hcp energies and will therefore not affect the dynamics of either system.

## III.   PATH INTEGRAL MOLECULAR DYNAMICS

The free energy $F^*$ of the quantum LJ system can be calculated from PIMD simulations by partitioning it into two components:

$$F^* = F_c^* + F_q^* \tag{6}$$

The classical free energy term $F_c^*$ can be calculated using the standard Einstein crystal method.[38–40] The excess quantum free energy $F_q^*$ term is obtained using mass thermodynamic integration, as outlined in the supplementary material. As this procedure is quite computationally expensive, it is not feasible to use it to fully explore the phase diagram of the quantum LJ solid. Instead, we chose to perform a full calculation of the quantum-corrected free energy for a single reference point $F_0^*(V_0^*, T_0^*)$ and then use Gibbs-Helmholtz integration of the free energy to generate the rest of the phase diagram. For a given $(V^*, T^*)$ point the free energy can be calculated from the reference point using the thermodynamic relationships

$$F^*(T^*; V^*) = T^* \left[ \frac{F_0^*}{T_0^*} - \int_{T_0^*}^{T^*} \frac{U^*(T^*)}{T^{*2}} dT^* \right] \tag{7}$$

for constant volume and

$$F^*(V^*; T^*) = F_0^* - \int_{V_0^*}^{V^*} P^*(V^*) dV^* \tag{8}$$

for constant temperature. PIMD trajectories must still be run to obtain values for $U^*(T^*)$ and $P^*(V^*)$, but only one trajectory is required for each point instead of a full mass thermodynamic integration.

### A.   PIMD computational details

Classical molecular dynamics and PIMD simulations were performed with LAMMPS[41] using the i-PI wrapper.[42] Simulations were run with $\sigma = 2.96$ Å and $\varepsilon = 0.00295$ eV,

6

parameters which have been shown to give good results for PIMC calculations of noble gas solids.[17,18] Systems of 256 Lennard-Jones particles with either the fcc or hcp crystal structures were initialized at a specified density $\rho^*$. Trajectories were then initiated in the $NVT$ ensemble with orthorhombic periodic boundary conditions. Temperature was kept constant using the stochastic PILE-G thermostat[43] with a relaxation time of 0.01 $t^*$. Simulations were run at temperatures ranging from $T^* = 0.10$ to 0.50 and $\rho^* = 0.65$ to 1.30, well below the melting curve for the classical LJ solid.[44,45] A timestep of 0.001 $t^*$ was used for all trajectories, and PIMD calculations were performed with 144 beads. For all phase diagrams the reference point was chosen to be at $T_0^* = 0.10$ and $\rho_0^* = 1.07255$, which is the zero-pressure density for the classical LJ solid.

## B.   Classical free energies

As a starting point for the PIMD calculations, we first determined the classical free energy term $F_c^*$ at the chosen reference point of $T_0^* = 0.10$ and $\rho_0^* = 1.07255$ using the standard Einstein crystal method.[38–40] The interaction cutoff $r_c^*$ was initially chosen to be 2.5, as it is the most popular choice in the literature. The sensitivity of the $F_c^*$ term to the choice of cutoff length $r_c^*$ was investigated by running simulations with $r_c^* = 2.2$ and 2.8 as well. The results are listed in Table II, with the phase stability expressed relative to the hcp phase as

$$\Delta F_c^* = F_{c,\text{hcp}}^* - F_{c,\text{fcc}}^*. \tag{9}$$

Predictably, the phase stability of the STS model is highly dependent on the chosen cutoff,[8,9] with $r_c^* = 2.2$ and 2.5 favouring hcp while 2.8 favours fcc. To reduce this cutoff effect the GSP correction to $\Delta F_c^*$ was calculated from the ground state fcc and hcp structures using Eqn. 4 as $\Delta U(\rho^*)_{\text{LRC}} = U_{\text{LRC}}^{\text{hcp}}(\rho_{\text{hcp}}^*) - U_{\text{LRC}}^{\text{fcc}}(\rho_{\text{fcc}}^*)$. The resulting correction term and corrected free energy difference $\Delta F_{c,\text{corr}}^* = \Delta F_c^* + \Delta U(\rho^*)_{\text{LRC}}$ is also listed in Table II. The net result is that the effect of the cutoff length is almost entirely eliminated in the GSP model, with all systems showing the same $\Delta F_{c,\text{corr}}^*$ within error and stabilization of hcp in all cases.

From here, the rest of the phase diagram up to $T^* = 0.5$ and $\rho^* = 1.30$ was calculated using Eqns. 7 and 8. For systems with different densities it was necessary to scale the cutoff length so that the same number of neighbour shells were included inside the cutoff for all

TABLE II. Classical free energy differences for the fcc and hcp phases in units of $\varepsilon$ per atom, obtained using thermodynamic integration at $T^* = 0.10$ and $\rho_0^* = 1.07255$. Negative values of $\Delta F_c^*$ indicate stability of the hcp phase. Results are shown for the spherically truncated and shifted (STS) model as well as the correction for the ground state perturbation (GSP model). Errors were obtained using block averaging.

| $r_c^*$ | STS | | | GSP | |
|---|---|---|---|---|---|
| | $F_{c,\text{fcc}}^*$ | $F_{c,\text{hcp}}^*$ | $\Delta F_c^*$ | $\Delta U(\rho^*)_{\text{LRC}}$ | $\Delta F_{c,\text{corr}}^*$ |
| 2.2 | $-5.33423(4)$ | $-5.33667(4)$ | $-0.00244(6)$ | $0.00152$ | $-0.00092(6)$ |
| 2.5 | $-5.86319(4)$ | $-5.87210(4)$ | $-0.00892(6)$ | $0.00797$ | $-0.00094(6)$ |
| 2.8 | $-6.18448(4)$ | $-6.17927(4)$ | $0.00521(6)$ | $-0.00618$ | $-0.00097(6)$ |

simulations. This was done relative to the reference point at $\rho_0^* = 1.07255$ as

$$r_c^*(\rho^*) = 2.5 \left( \frac{1.07255}{\rho^*} \right)^{1/3}. \tag{10}$$

The resulting phase diagrams are shown in Figure 1 for both the STS and GSP models. The STS model shows that hcp is stable at low densities and is in agreement with previous assessments of the phase behaviour of the uncorrected $r_c^* = 2.5$ LJ solid.[37] Inclusion of long-range GSP correction shifts the phase boundary by stabilizing fcc over hcp, and as such the hcp phase is only stable at low density and temperature. Since the fcc phase has been shown to have higher entropy than the hcp phase,[46–50] it is then perhaps unsurprising that inclusion of long-range order works to stabilize fcc. All in all, these results demonstrate the delicate balance between solid phases and the surprising complexity in this simple model. Further information about the phase stability may be gleaned from a consideration of finite size effects, but this is beyond the scope of this work.

## C. Quantum free energies

The excess quantum free energies $\Delta F_q^*$ for each phase were obtained from PIMD using a 13-point mass thermodynamic integration from $m = m_0$ to $m = \infty$ at the chosen reference point $T_0^* = 0.10$, $\rho_0^* = 1.07255$. The free energy difference

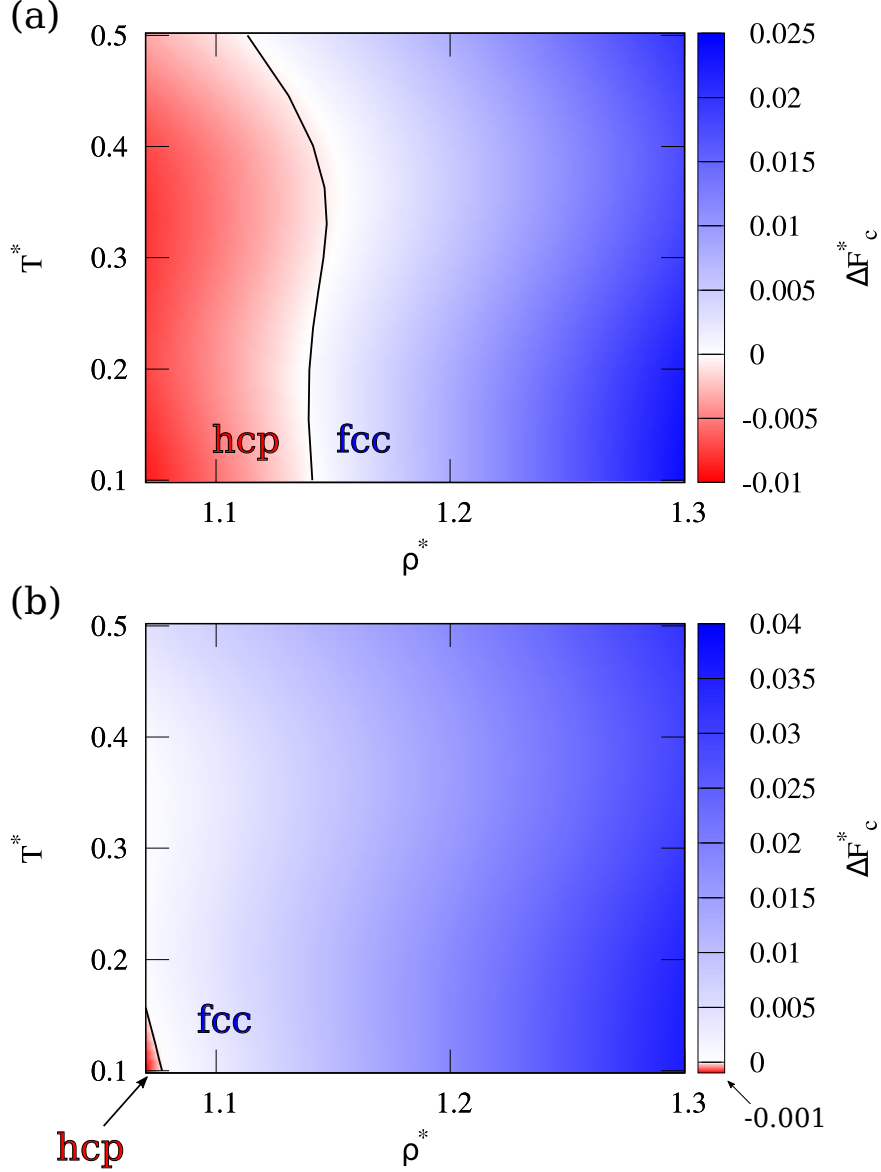$$\Delta\Delta F_q^* = \Delta F_{q,\text{hcp}}^* - \Delta F_{q,\text{fcc}}^* \tag{11}$$

8

FIG. 1. Phase diagrams for the classical LJ solid obtained using thermodynamic integration for (a) the STS model and (b) the GSP-corrected model. Red regions indicate hcp stability, and blue corresponds to fcc.

between the two phases was monitored and trajectories 150-200 $t^*$ in length were required for adequate convergence of this quantity. An example is shown in Figure 2. Five $m_0$ values were chosen such that the solid ranged in quantumness from $\Lambda^* = 0.1$ to 0.4 ($m_0 = 20$ amu to 1 amu for the $\sigma$ and $\epsilon$ values used in this work).

The phase stability of the quantum LJ solid was then calculated using Eqns. 7 and 8 with $F_0^* = F_c^* + \Delta F_q^*$ at the reference point of $T_0^* = 0.10$, $\rho_0^* = 1.07255$. For each $\Lambda^*$
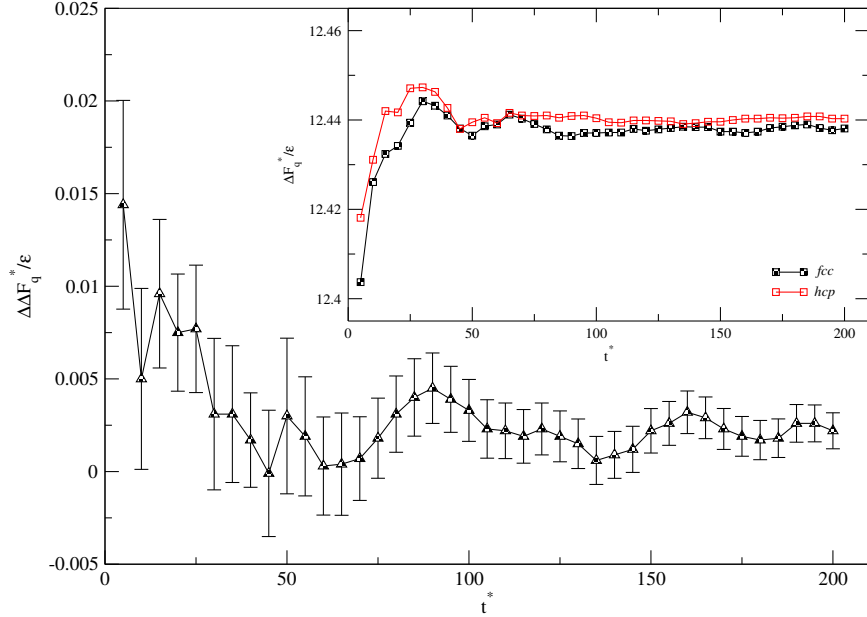
FIG. 2. Convergence of $\Delta\Delta F_q^*$ with respect to PIMD trajectory length for $T^* = 0.10$ and $m_0 = 1$. An initial equilibration period of 5 $t^*$ is not included in this plot. The inset shows the convergence of the individual fcc and hcp $\Delta F_q^*$ values.

value, calculations were run from $\rho^* = 1.30$ to whichever density gave $P^* \approx 0$. Note that only densities where the system remained solid across the whole temperature range were considered here, thus in some cases it was not possible to reach $P^* \approx 0$ due to melting at higher temperature. The resulting phase diagrams are shown in Figure 3 for both the STS and GSP models. Phase stability is represented as $\Delta F^* = F_{\text{hcp}}^* - F_{\text{fcc}}^*$.

The quantum contribution to the pressure is immediately apparent in these plots, since the highly quantum systems require significantly lower densities to reach $P^* \approx 0$ than in the classical case. Even though the GSP model favours fcc more than the STS model, the inclusion of nuclear quantum effects stabilizes hcp over fcc in both cases. This is evidenced by the increase in size of the hcp region with increasing quantumness, which is observed even with a relatively heavy particle at $\Lambda^* = 0.1$. Since these phase diagrams are plotted against $\rho^*$, this growth of the hcp region means that the fcc region is being pushed to higher and higher pressures with increasing quantumness and is therefore being destabilized relative to hcp. Interestingly, the slope of the phase boundary changes sign at $\Lambda^* = 0.4$. This may be due to fluctuations in this highly quantum system, or it may indicate a change in the nature of the phase boundary at high quantumness.
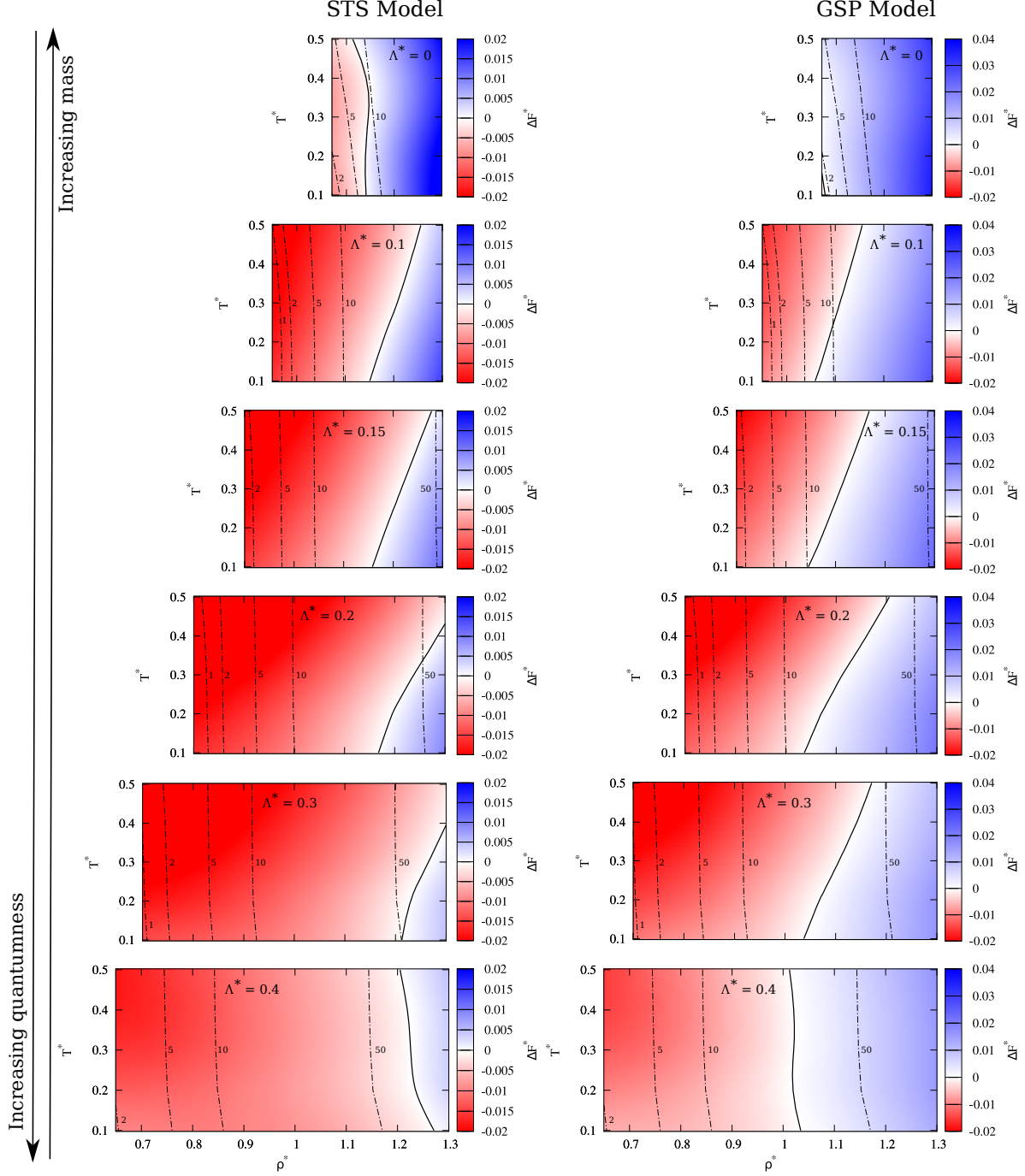
10

FIG. 3. Phase diagrams for the quantum LJ solid. As in Figure 1, red regions correspond to hcp stability and blue correspond to fcc stability. The STS model is shown on the left, and the GSP model on the right. The columns are arranged in order of increasing quantumness, with $\Lambda^* = 0$ at the top and $\Lambda^* = 0.4$ at the bottom. Dashed lines correspond to isobars for the hcp phase at $P^* = 1, 2, 5, 10$ & $50$. Isobars for the fcc phase are indistinguishable from the hcp phase on the scale of this plot.

## IV. QUASI-HARMONIC LATTICE DYNAMICS

An alternative assessment of the free energy of the quantum LJ system was obtained using QHLD. This technique involves using the phonon density of states to calculate physical quantities such as free energy or pressure. QHLD relies on the harmonic approximation and so is less accurate than the PIMD, however decomposition into individual phonon modes provides valuable insight. In QHLD, the free energy difference between hcp and fcc phases $\Delta F^* \equiv F^*_{\text{hcp}} - F^*_{\text{fcc}}$ is expressed as:

$$\Delta F^* = \Delta U^*_{GS} + \Delta F^*_{\text{zp}} + \frac{k_B T^*}{N} \sum_{i=1}^{3N} \ln \left[ \frac{1 - e^{-\beta \hbar \omega_i^{\text{hcp}}}}{1 - e^{-\beta \hbar \omega_i^{\text{fcc}}}} \right], \tag{12}$$

where $\Delta U^*_{GS}$ is the ground state energy of the crystal and $\omega_i^{\text{hcp(fcc)}}$ denotes the angular frequency of the $i$th phonon for the hcp(fcc) crystal. $\Delta F^*_{\text{zp}}$ is the zero-point contribution to the free energy difference:

$$\Delta F^*_{\text{zp}} = \frac{3}{2} \hbar \left( \langle \omega^{hcp} \rangle - \langle \omega^{fcc} \rangle \right) \tag{13}$$

where the angled brackets denote the mean phonon frequency. In the classical limit, $\Delta F^*_{zp} = 0$ and Eqn 12 becomes:

$$\Delta F^* = \Delta U^*_{GS} + 3k_B T^* \Delta \langle \ln \omega \rangle \tag{14}$$

In the quantum zero-temperature limit, Eqn 12 simplifies to:

$$\Delta F^* = \Delta U^*_{GS} + \Delta F^*_{\text{zp}} = \Delta U^*_{GS} + \frac{3}{2} \hbar \Delta \langle \omega \rangle \tag{15}$$

The above equations can be used to determine $\Delta F^*$ at a given $\rho^*$ and $T^*$ from the hcp and fcc phonon densities of states at $\rho^*$. By considering many $\rho^*$ and $T^*$, the regions of the $\rho^*$–$T^*$ phase diagram where hcp is stable ($\Delta F^* < 0$) and where fcc is stable ($\Delta F^* > 0$) can be deduced. Moreover, it is also possible to use the hcp and fcc densities of states over a range of $\rho^*$ to determine the $P^*$–$T^*$ phase diagram. This is achieved by first calculating the hcp and fcc Gibbs free energies as functions of $P^*$ and $T^*$ via

$$G^*(P^*, T^*) = F^*(\rho^{*\prime}, T^*) + P^*(\rho^{*\prime}, T^*)/\rho^* \tag{16}$$

where $\rho^{*\prime}$ in this expression is the $\rho^*$ such that $P^*(\rho^{*\prime}, T^*) = P^*$, and

$$P^*(\rho^*, T^*) = \rho^{*2} \left( \frac{\partial F^*}{\partial \rho^*} \right)_T \tag{17}$$

is the pressure at a given $\rho^*$ and $T^*$. Then, the Gibbs free energy difference $\Delta G^* = (G^*_{\mathrm{hcp}} - G^*_{\mathrm{fcc}})$ is evaluated as a function of $P^*$ and $T^*$. Finally, $\Delta G^*(P^*, T^*)$ is used to deduce the hcp and fcc regions of the $P^*$–$T^*$ phase diagram similarly to above for the $\rho^*$–$T^*$ phase diagram: $\Delta G^* < 0$ indicates that hcp stable; $\Delta G^* > 0$ that fcc is stable.

## A.   QHLD computational details

For our QHLD calculations we used the code GULP[51] to calculate phonon density of states (DoS); and to calculate static crystal energies we used the lattice-sum-based expressions provided in ref. 3. In the GULP calculations we employed a 12-atom orthorhombic unit cell for both hcp and fcc. The hcp unit cell corresponded to six planes stacked in the $z$-direction, with two particles per plane, and a stacking sequence of ABABAB. The fcc unit cell was the same except the stacking sequence was ABCABC, this ensures both structures have the same reduced Brillouin zone. The accuracy and precision of the DoS output by GULP is determined by how many k-points, $N_{\mathrm{k\text{-}points}}$, are used in sampling the Brillouin zone, and how many bins $N_{\mathrm{bins}}$ are used in the DoS histogram – which is the key output by GULP for our purposes. We performed preliminary calculations at $\rho^* = 0.8, 1.07255$ and $1.3$ in order to determine appropriate values for these parameters, and found that a Monkhorst-Pack scheme with 40 grid points along each dimension of the Brillouin zone, and 300,000 bins in the DoS histogram, was sufficient. To elaborate, these parameters yielded an error for $\Delta\langle\omega\rangle$ (associated with numerical integration over the DoS histogram) which was significantly less than $|\Delta\langle\omega\rangle|$, ensuring that the calculations had sufficient precision to distinguish which of hcp and fcc was stable according to the zero-point energy. These parameters also yielded values for $\Delta\langle\omega\rangle$ which were converged with respect to both $N_{\mathrm{k\text{-}points}}$ and $N_{\mathrm{bins}}$. Finally, we note that we found it necessary to modify GULP's source code for this work. Specifically, we increased the number of significant figures used in the output file containing the DoS histogram; the default output format lacked the precision to reduce the error in $\Delta\langle\omega\rangle$ to what was required for this work.

## B. Initial investigations

The hcp and fcc phonon density of states (DoS) for $r_c^* = 10.0$ at $\rho^* = 1.07255$, the density for the classical LJ solid at $T^* = P^* = 0$, are shown in Figure 4. The figure shows that the hcp DoS has both low and high frequency peaks, while fcc has more intermediate frequency modes. Moreover, both structures share the same peak at high frequency, though the high-frequency peak is larger in fcc than hcp. However, despite the qualitatively different shapes of the densities of states of the two crystals, the mean frequencies and mean log-frequencies, which, as shown in Eqns 14 and 15, play an important role in determining which of the structures is stable, are indistinguishable on the scale of this figure. Hence the fine structure of the DoS must be considered to determine which of hcp and fcc is stable. We return to this point in a moment.
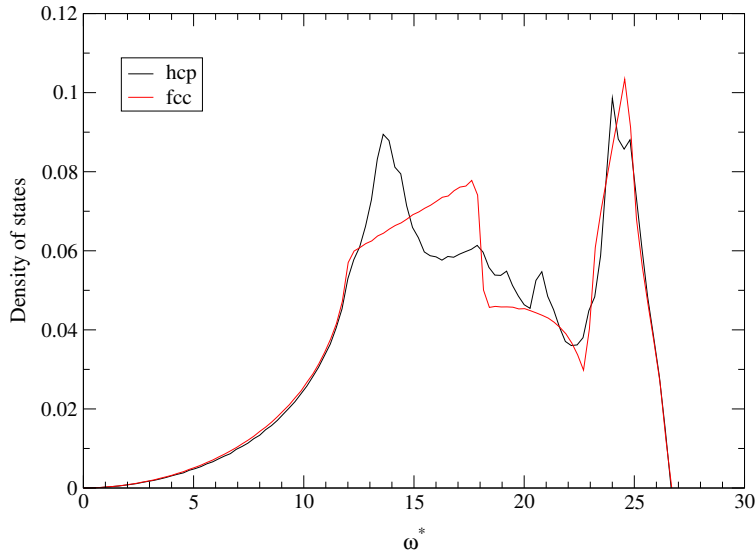


FIG. 4. Phonon density of state for the hcp and fcc structures at $\rho^* = 1.07255$ for the LJ solid with $r_c^* = 10.0$.

Preliminary calculations revealed that the hcp and fcc crystals were mechanically unstable for densities less than $\rho^* = 0.8$: at these densities the system exhibited phonons with imaginary frequencies for all cutoffs considered. Hence, keeping in mind that we are interested in the low pressure region of the phase diagram, we focused on densities ranging from $\rho^* = 0.8$ to 1.3.

The hcp pressure is shown as a function of $T^*$ over this density range for various $\Lambda^*$ in Figure 5. The fcc pressure is indistinguishable from that of hcp on the scale of this figure. As expected, increasing the quantumness while fixing the density results in an increase in the pressure of the system. This is primarily due to zero-point vibrations. To elaborate, using Eqn. 17, in conjunction with the fact that the zero-point energy is $F_{zp}^* = 3\hbar\langle\omega\rangle/2$ (c.f. Eqn. 13), the contribution to the pressure from this energy is

$$P_{zp} = \rho^2 \left( \frac{\partial F_{zp}}{\partial \rho} \right)_T = \frac{3}{2}\rho^2 \frac{\partial \langle \hbar\omega \rangle}{\partial \rho}. \tag{18}$$

Noting that $\partial\langle\hbar\omega\rangle/\partial\rho$ is positive and proportional to $\hbar/\sqrt{m}$, and hence also $\Lambda^*$, it follows that $P_{zp}$ is also proportional to $\Lambda^*$. Figure 5 also reveals that for $\Lambda^* = 0.2$, 0.3 and 0.4 there is no *mechanically stable* hcp or fcc density corresponding to $P = 0$ in the quasi-harmonic approximation: the figure implies that the hcp and fcc densities for $P = 0$ would be achieved at $\rho < 0.8$, which, as just mentioned, are mechanically unstable within the approximation.
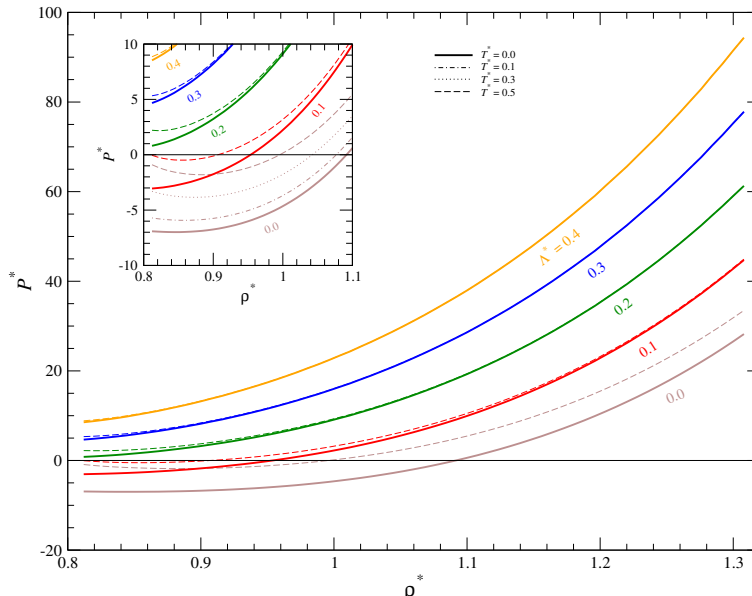


FIG. 5. $P^*$ vs. $\rho^*$ for the hcp phase of the LJ solid ($r_c^* = 10$) obtained from QHLD for various $\Lambda^*$ and $T^*$. The inset shows the low density region in more detail.

To validate our implementation of QHLD we also considered $\Lambda^* = 0.0103$, 0.0166, 0.0296 and 0.0896, which correspond to Xe, Kr, Ar and Ne respectively,[16] and compared results for $r_c^* = 10$ to those of ref. 16. Plots of $P^*$ vs. $\rho^*$ for these $\Lambda^*$ at $T^* = 0$ (not shown) were in good agreement with those given in ref. 16, as were plots of $\rho^*$ vs. $T^*$ at $P^* = 0$ (not

shown).

## C. Sensitivity to cutoff

To investigate the sensitivity of the phase behaviour to $r_c^*$, we focused on $\rho^* = 1.07255$. We considered $r_c^* = 2.2$, 2.5 and 2.8, supplementing our calculations described above for this density using $r_c^* = 10$. The hcp and fcc DoS for $r_c^* = 2.2$, 2.5 and 2.8 are almost identical to those shown in Figure 4 (which recall are for $r_c^* = 10$) on the scale of the figure. However, differences in the fine structure of the DoS for different $r_c^*$ have important implications for the stability of hcp vs. fcc.

Recall that in the zero-temperature limit $\Delta F$ depends on the zero-point energy through the difference in the mean phonon frequencies $\Delta\langle\omega\rangle \equiv (\langle\omega\rangle_{\text{hcp}} - \langle\omega\rangle_{\text{fcc}})$ (Eqn. 15), while in the classical limit $\Delta F$ depends on the difference in the mean log-frequencies $\Delta\langle\ln\omega\rangle$ (Eqn. 14). In Table III $\Delta\langle\omega^*\rangle$ and $\Delta\langle\ln\omega^*\rangle$ are compared for various values of $r_c^*$. It can be seen that $\Delta\langle\ln\omega^*\rangle$ is positive for all $r_c^*$. This implies that vibrational effects act to stabilise fcc in the classical limit for all considered $r_c^*$. This follows from Eqn. 14: if $\Delta\langle\ln\omega^*\rangle > 0$, $\Delta F^*$ increases with $T$, which corresponds to fcc stabilisation.

By contrast, the sign of $\Delta\langle\omega^*\rangle$ depends on $r_c^*$. $\Delta\langle\omega^*\rangle$ is negative at $r_c^* = 2.2$, implying that the zero-point energy of hcp is lower than that of fcc. Since increasing quantumness increases the size of the zero-point contribution to $\Delta F^*$ (c.f. Eqn. 13), this means that increasing quantumness stabilises hcp for $r_c^* = 2.2$ (in the zero-temperature limit). On the other hand, for $r_c^* = 2.5$, $\Delta\langle\omega^*\rangle$ is positive, which implies the opposite, i.e. that fcc is stabilised by quantum effects. The same is true for $r_c^* = 2.8$ and $r_c^* = 10.0$, though for these cutoffs $\Delta\langle\omega^*\rangle$ is of a smaller magnitude and hence the stabilisation of fcc by quantum effects is less pronounced than at $r_c^* = 2.5$.

The above discussion is borne out in Figure 6, which shows $\Delta F^*$ vs. $\Lambda^*$ at this density for various $T^*$ and $r_c^*$. Note that for $T^* = 0$ increasing the quantumness increases $\Delta F^*$ for $r_c^* = 2.5$, 2.8 and 10.0, with a more pronounced increase for $r_c^* = 2.5$; while increasing quantumness decreases $\Delta F^*$ for $r_c^* = 2.2$. These trends are in accordance with the values of $\Delta\langle\omega^*\rangle$ for each cutoff described above. Note also that, at $\Lambda^* = 0$, increasing $T^*$ increases $\Delta F^*$, in accordance with the above discussion that $\Delta\langle\ln\omega^*\rangle$ is positive for all $r_c^*$, i.e. that vibrational effects always stabilise fcc in the classical limit. This is also the case away from

16

TABLE III. Differences in the phonon mean frequencies and mean log-frequencies between the hcp and fcc structures, i.e. $\Delta\langle\omega^*\rangle$ and $\Delta\langle\ln\omega^*\rangle$, for the LJ solid at $\rho^* = 1.07255$ and various cutoffs $r_c^*$. A positive value indicates that $\Delta\langle\omega^*\rangle$ or $\Delta\langle\ln\omega^*\rangle$ is higher for the hcp structure than for the fcc structure.

| $r_c^*$ | $\Delta\langle\omega^*\rangle$ | $\Delta\langle\ln\omega^*\rangle$ |
|---|---|---|
| 2.2 | -0.0012 | 0.0005 |
| 2.5 | 0.0102 | 0.0013 |
| 2.8 | 0.0021 | 0.0008 |
| 10.0 | 0.0033 | 0.0009 |

the classical limit: *thermal effects* always act to stabilise fcc.

A key result to be drawn from the above discussion is that the difference in the zero-point energies of the hcp and fcc structures in the LJ solid is highly sensitive to $r_c^*$, to the point that changing $r_c^*$ can reverse whether hcp or fcc is stablised by increasing the quantumness of the system. There is no analogous problem in the classical case; the discussion above, and previous studies, have revealed that changing $r_c^*$ does not change the fact that the fcc structure is stabilised by thermal effects.

## D. Phase behaviour

We now consider the phase behaviour for $r_c^* = 10$ over the density range $\rho^* = 0.8$ to 1.3. $\Delta F^*$ vs. $\rho^*$ is shown in Figure 7 for various $\Lambda^*$. The figure shows that increasing quantumness generally has the effect of stabilising fcc: as $\Lambda^*$ is increased, $\Delta F^*$ also increases. The effect on the phase diagram is shown in Figure 8, which shows the hcp-fcc phase boundaries for various $\Lambda^*$ in the $\rho^*$–$T^*$ plane. Note that increasing quantumness has the effect of reducing the size of the hcp region; the hcp region of the phase diagram is "compressed" towards $\rho^* = 0.8$ as $\Lambda^*$ is increased.

This behaviour is largely due to the zero-point energy. Recall that for $r_c^* = 10$ we found for $\rho^* = 1.07255$ that the zero-point energy favours fcc: $\Delta F_{ZP}^* > 0$. The same is true at all other densities we considered. As the quantumness is increased, $\Delta F_{ZP}^*$ becomes a larger contribution to $\Delta F^*$, and therefore fcc becomes increasingly favoured. This is especially
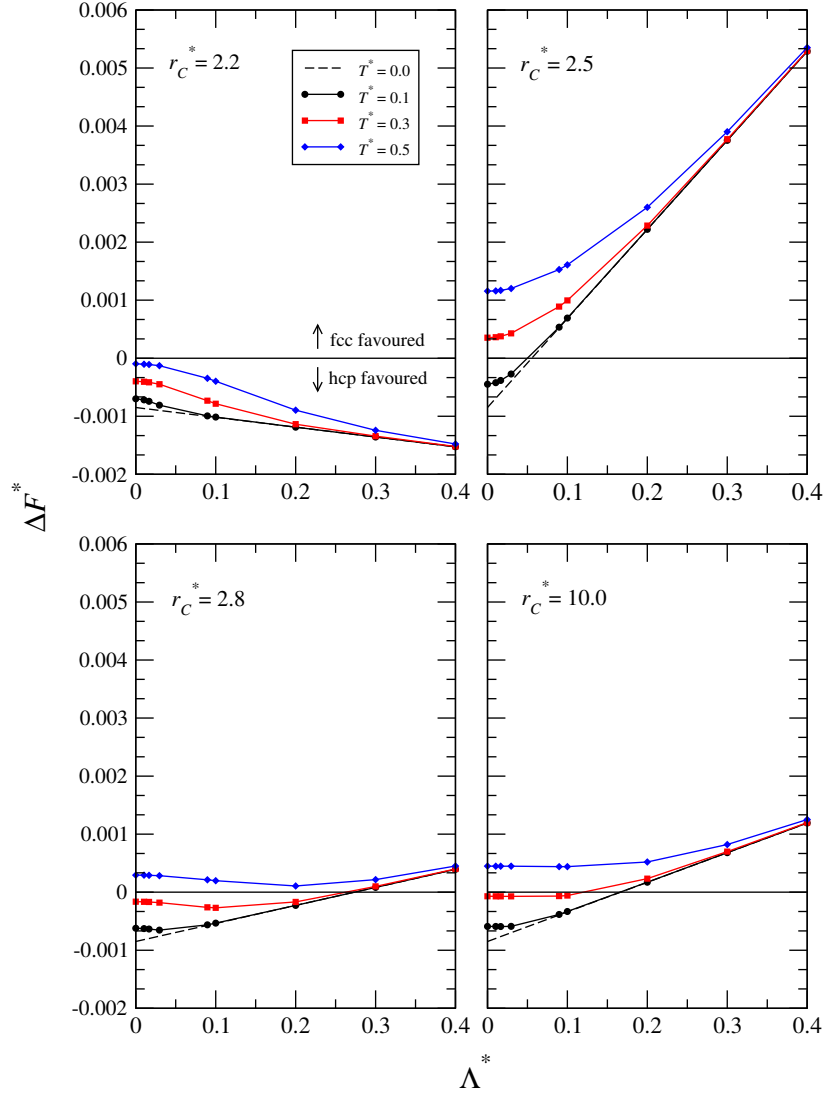
FIG. 6. hcp-fcc free energy difference, $\Delta F$, from QHLD vs. de Boer parameter, $\Lambda^*$, for the LJ solid at $\rho^* = 1.07255$. Each panel corresponds to a different cutoff $r_c^*$.

true at high densities, where, as shown in Figure 7, $\Delta F_{ZP}^*$ is larger than at lower densities, leading to a more pronounced effect.

Of course, temperature also affects $\Delta F^*$ through the difference in the vibrational energies. At low pressures $\Delta F_{ZP}^*$ is smaller and temperature plays a larger role. At very low densities the phase behaviour is non-trivial: at $\rho^* = 0.84$ as $\Lambda^*$ is increased there is an increase in the hcp-fcc transition temperature until $\Lambda^* = 0.2$, followed by a decrease as $\Lambda^*$ is increased
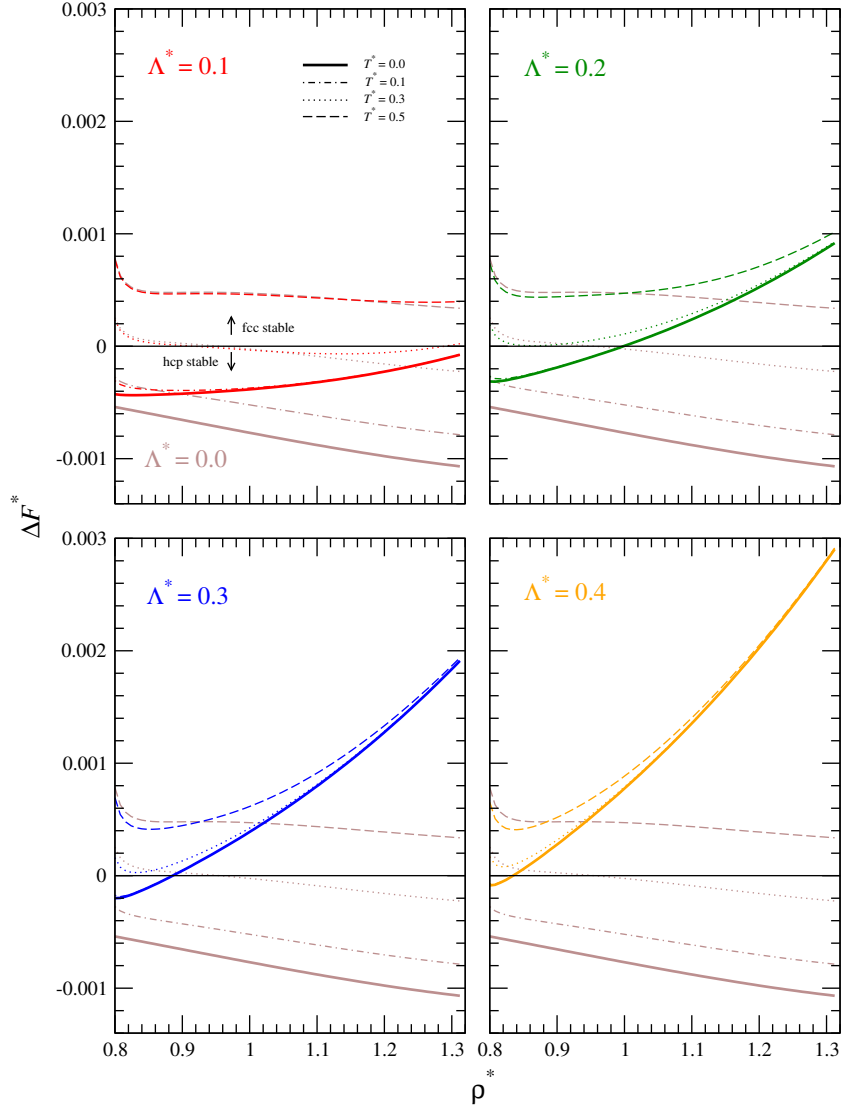
18

FIG. 7. hcp-fcc free energy difference $\Delta F$ vs. $\rho$ for the LJ solid at $r_c^* = 10$ obtained from QHLD, for various $T^*$ and $\Lambda^*$.

further.

As can be seen from Figure 5, much of the range covered in Figures 7 and 8 pertain to densities which correspond to negative pressures. $\Delta G^*$ vs. $P^*$ is shown in Figure 9, and the hcp-fcc phase boundaries in the $P^*$–$T^*$ plane are shown in Figure 10. Recall that neither crystal structure is mechanically stable at $P^* = 0$ for $\Lambda^* \gtrsim 0.2$ in the quasi-harmonic approximation, which is why not all the curves in these figures extend to $P^* = 0$. Figure 10
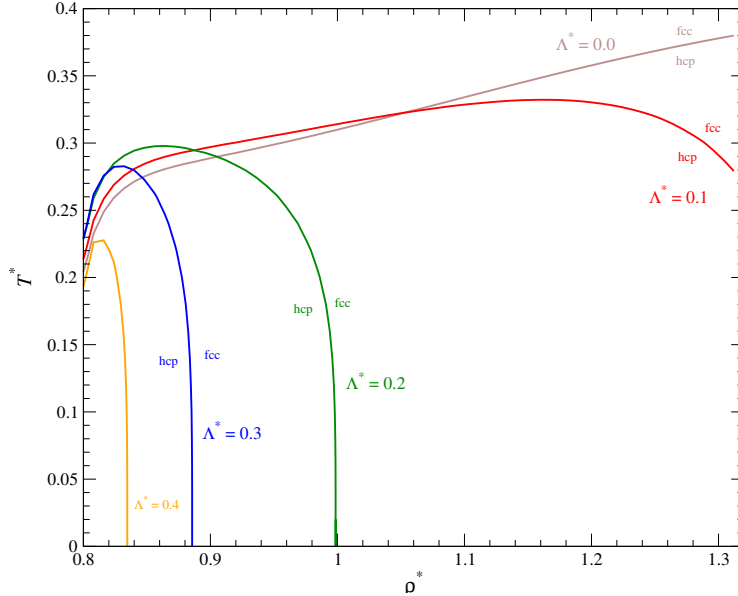
FIG. 8. Phase diagram of the LJ solid in the $\rho^*$-$T^*$ plane, for various $\Lambda^*$, determined using QHLD and $r_c^* = 10$.

reveals that as the quantumness is increased the location of the hcp-fcc transition is moved to lower pressures. Moreover, at $P^* = 0$, increasing $\Lambda^*$ from 0 to 0.1 moves the $P^* = 0$ transition temperature to lower temperatures; the size of the region of hcp stability is reduced upon moving from $\Lambda^* = 0$ to $\Lambda^* = 0.1$. Interestingly, for $\Lambda^* = 0.4$ there are no pressures at which hcp is thermodynamically stable. Hence no phase boundary exists in the quasi-harmonic approximation for $\Lambda^* = 0.4$; the only stable phase is fcc.

## V. DISCUSSION

### A. Reconciling the two methods

Our PIMD and QHLD calculations make qualitatively different predictions for the phase behaviour of the quantum LJ solid. At $P^* \approx 0$ the classical LJ solid exhibits a phase transition from the hcp phase (stable at $T^* = 0$) to the fcc phase at $T^* \approx 0.3$. Our QHLD results suggest that this is also the case in the quantum solid for $\Lambda^* \lesssim 0.2$. However, our PIMD results suggest that hcp is stable at $P^* \approx 0$ for all temperatures up to at least $T^* = 0.5$. Another clear discrepancy between the two methods arises with regards to the phase behaviour at low temperatures. QHLD implies that at $T^* \approx 0$ the hcp-fcc transition
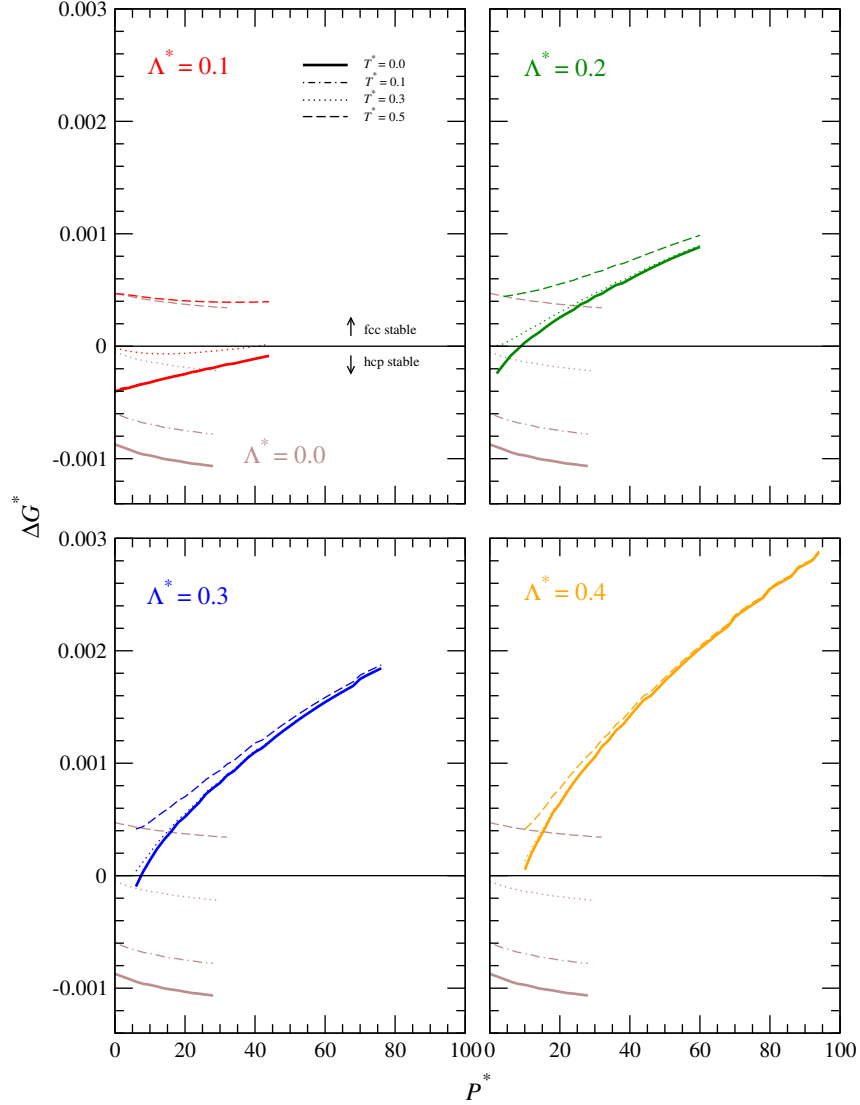
FIG. 9. hcp-fcc free energy difference $\Delta G^*$ vs. $P^*$ for the LJ solid at $r_c^* = 10$ obtained from QHLD, for various $T^*$ and $\Lambda^*$.

moves to lower densities as the quantumness is increased, going as low as $\rho^* = 0.835$ at $\Lambda^* = 0.4$. By contrast the PIMD transition density never drops below $\rho^* = 1.0$ (see Figures 3 and 8). Finally, the hcp-fcc free energy differences obtained from PIMD are typically about an order of magnitude larger than those obtained from QHLD (see Figures 3 and 7).

There are a number of possible causes for the discrepancies between the two methods. Firstly, the models used in the QHLD and PIMD calculations were different: the QHLD
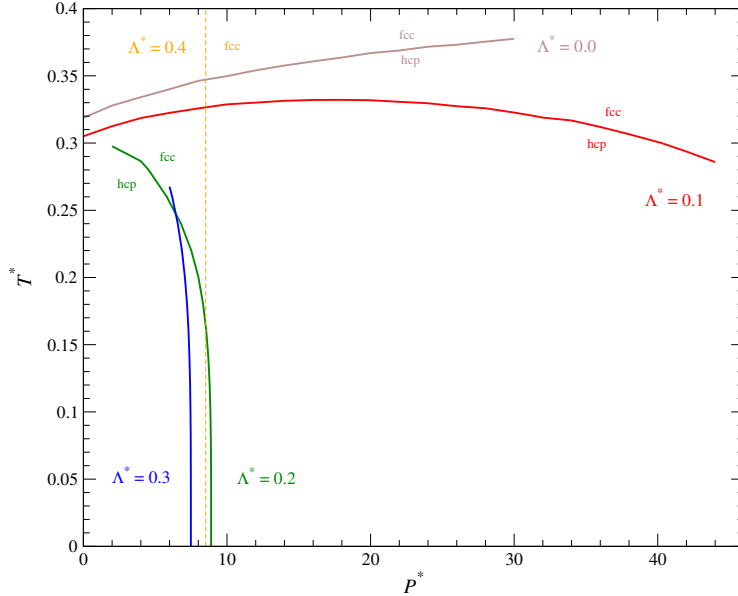
FIG. 10. Phase diagram of the LJ solid in the $P^*$-$T^*$ plane, for various $\Lambda^*$, determined using QHLD and $r_c^* = 10$. Solid lines correspond to phase boundaries for $\Lambda^* = 0.0$, 0.1, 0.2 and 0.3. No phase boundary exists for $\Lambda^* = 0.4$; the fcc phase is stable for all realisable pressures. The lower bound for the realisable pressures for $\Lambda^* = 0.4$ is indicated by a dashed line.

calculations employed $r_c^* = 10$, while the PIMD calculations used a value of $r_c^*$ which scaled commensurately with the density (Eqn. 10). To investigate this further, we repeated our QHLD calculations using the same cutoff scheme used in our PIMD calculations. However, we found that this *worsened* the agreement between the two methods: using the scaled cutoff scheme makes the fcc *more* stable in the quasi-harmonic approximation than it is for $r_c^* = 10$. This can be seen by comparing Figures 7 and 11, the latter of which shows $\Delta F$ vs. $\rho^*$ using the scaled cutoff scheme. Another key difference between our QHLD and PIMD calculations is that they pertain to different system sizes, namely $N = \infty$ and $N = 256$ particles, respectively. It is well known that the quantitative details of the phase diagram for the classical LJ solid are sensitive to the system size, and surely the same is true for the quantum solid. However, we do not believe that finite size effects are the main cause of the discrepancies. Rather, the main cause is the approximations which underpin the two methods.

A key difference between PIMD and QHLD is that the former takes into account anharmonic effects. It is well known that anharmonic effects play an important role in quantum
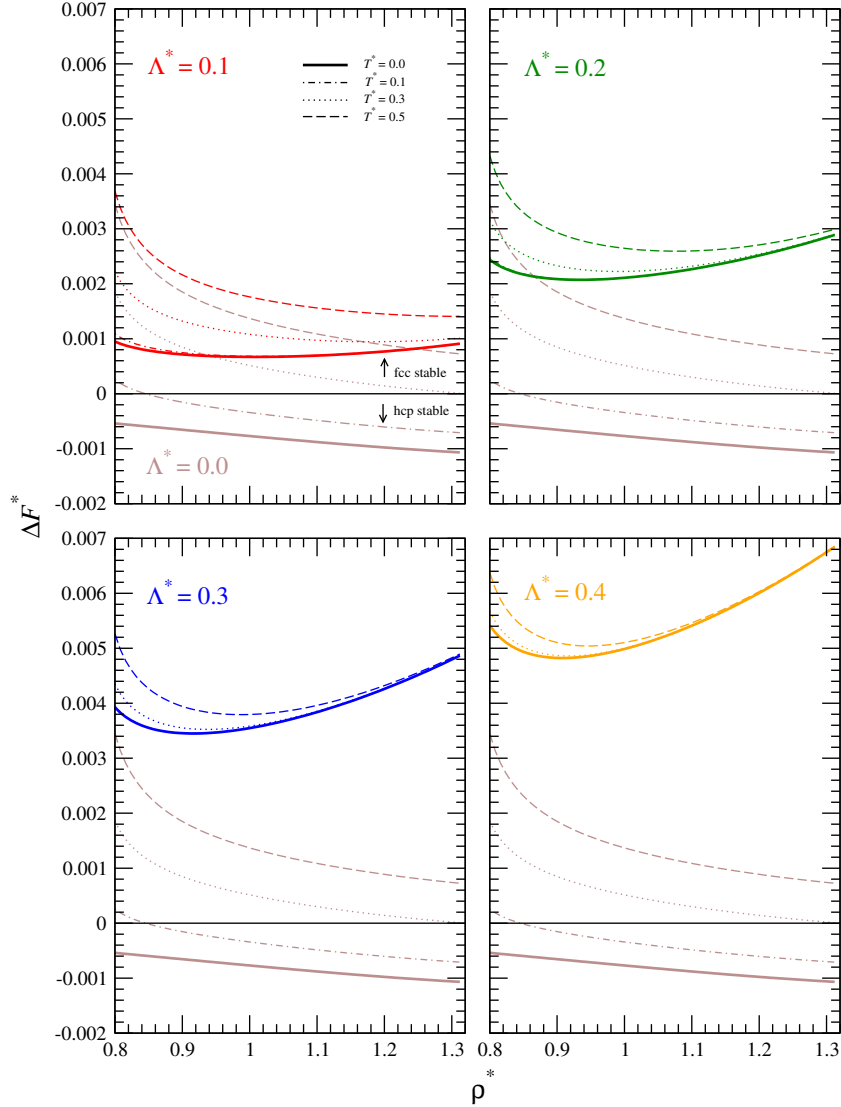
FIG. 11. hcp-fcc free energy difference $\Delta F^*$ vs. $\rho^*$ for the LJ solid obtained from QHLD using the cutoff scheme described by Eqn. 10, for various $T^*$ and $\Lambda^*$.

crystals.[26] Hence we expect that anharmonic effects are the main reason for the discrepancy between the PIMD and QHLD results. The breakdown of QHLD due to anharmonic effects even extends to low temperatures: anharmonic effects have been found to be significant even at zero temperature in the noble gas solids.[21,25] This brings into question the accuracy of our QHLD results at low temperatures. Interestingly, while the anharmonic contribution to the *total* free energy has been found to be significant at zero temperature,[21,25] the significance

of the anharmonic contribution to the hcp-fcc free energy *difference* is still somewhat an open question. It has been suggested that this contribution is negligible.[25] If this were true, then our QHLD prediction that fcc is stabilised by quantum effects at low temperatures would remain valid. One way of reconciling this with our finding that hcp is stabilised by quantum effects at high temperatures (implied by our PIMD results, which recall do not extend to temperatures as low as we considered with QHLD) would be if the phase diagram exhibited a re-entrant fcc-hcp-fcc transition at low pressures for highly quantum LJ systems, as illustrated schematically in Figure 12.
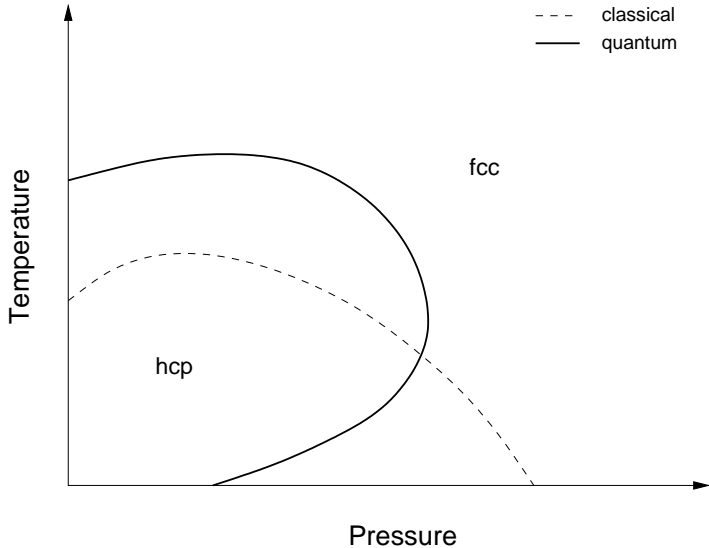


FIG. 12. Schematic phase diagrams of the classical LJ solid, and a speculative quantum LJ solid where the fcc phase is re-entrant at moderate pressures.

## B.    Origin of hcp stabilisation in PIMD

The origin of the fcc stabilisation with increased quantumness in QHLD was shown to be due to its lower mean vibrational frequency and thus lower zero point energy. The origin of hcp stabilization in PIMD is less clear, due to the opaque nature of PIMD simulations. To investigate this further we partition the $\Delta F^*$ values from Figure 3 into contributions from internal energy and entropy. The average difference in internal energy $\Delta E^*$ can be extracted

directly from the PIMD trajectories and so $-T^*\Delta S^*$ is easily accessible as:

$$-T^*\Delta S^* = \Delta F^* - \Delta E^* \tag{19}$$

The results are shown in Figure 13 for the cases of $\Lambda^* = 0$, 0.1 and 0.3 at the reference temperature $T^* = 0.1$. Here we only consider the GSP-corrected model, as we do not wish to include fluctuations in the energy due to cutoff effects. The $\Delta F^*$ curve is reminiscent of the QHLD result in Figures 7 and 11, but larger in magnitude and shifted to more dramatically favour hcp at low densities. From these plots we can clearly see that $\Delta E^*$, which contains the zero point energy, is practically negligible and that the free energy difference between the two phases is due to the difference in entropy $-T^*\Delta S^*$. Therefore the stabilization of quantum hcp in PIMD must be due to anharmonic effects which are not accounted for in QHLD.

## C.   Implications for noble gases

The LJ potential is often used to model interactions in noble gas solids and it is therefore interesting to consider our results in that context. Of the noble gases, only He has been observed in the hcp phase; all others adopt the fcc structure.[52,53] Explanations for this phenomenon have been offered in the literature[54–56] but a consensus has not been reached. In Figure 14 we compare the values of the de Boer parameter $\Lambda^*$ for the noble gases with our PIMD results for the GSP-corrected model.

By and large these results agree with the experimental observations. The heavy noble gases (Ar, Kr and Xe) are clustered near the fcc phase, while He has a strong preference for hcp. The only discrepancy is Ne, which is shown to prefer hcp with this treatment but has an fcc structure in reality. However, the LJ potential is a somewhat simplistic treatment and a more realistic potential which includes many-body effects may show more accurate phase behaviour for Ne. Overall, our results show that the hcp structure of He is due to quantum effects, while the heavy noble gases prefer the classically-favoured fcc structure. Moreover, there are very large contributions of zero-point vibrations to the pressure, in the case of helium these are large enough to drive the density below the region in which the Lennard-Jones potential can stabilize a crystal structure.
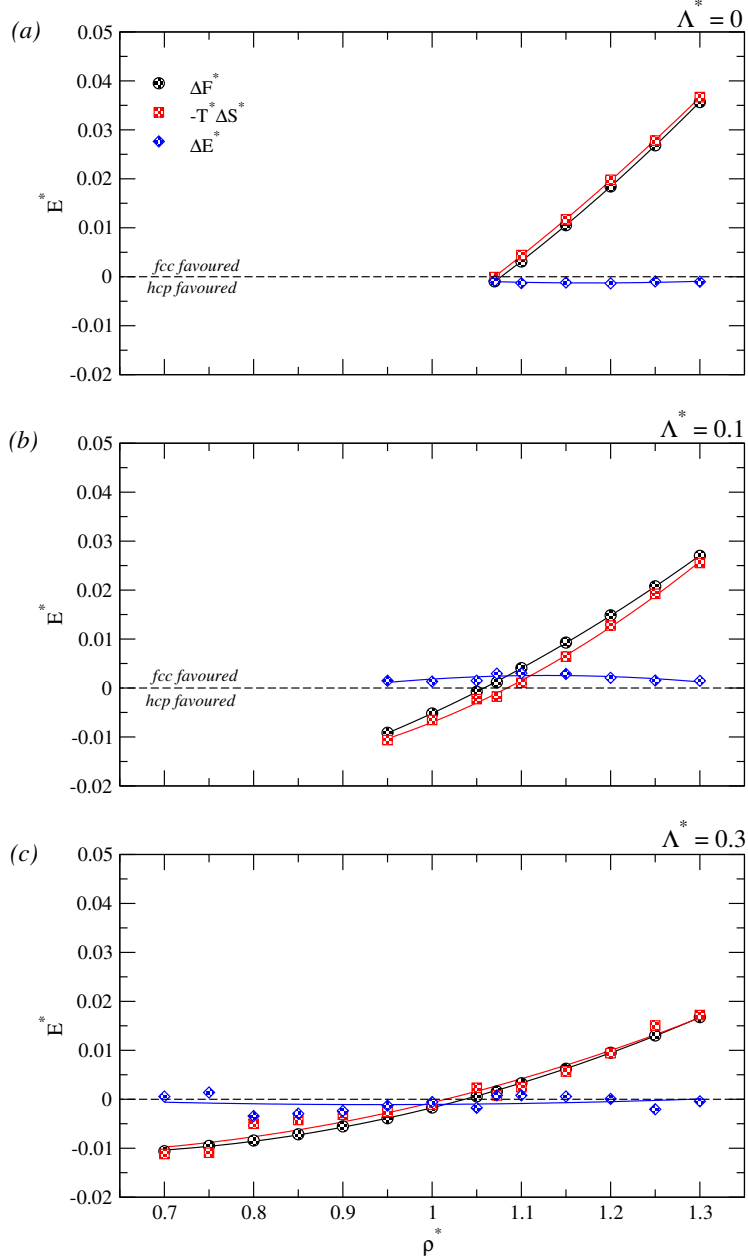
FIG. 13. Contributions of entropy and internal energy to phase stabilization in the GSP-corrected model at $T^* = 0.10$ for (a) $\Lambda^* = 0$ (classical system), (b) $\Lambda^* = 0.1$ and (c) $\Lambda^* = 0.3$. Negative values indicate stabilization of hcp and positive values indicate stabilization of fcc. Lines are quadratic fits to the data and are used to guide the eye.

## D. Prospect of other phases

One key conclusion of our QHLD calculations was that $P = 0$ was inaccessible for $\Lambda \gtrsim 0.3$ on account of the mechanical instability of the fcc and hcp crystals at very low pressures.
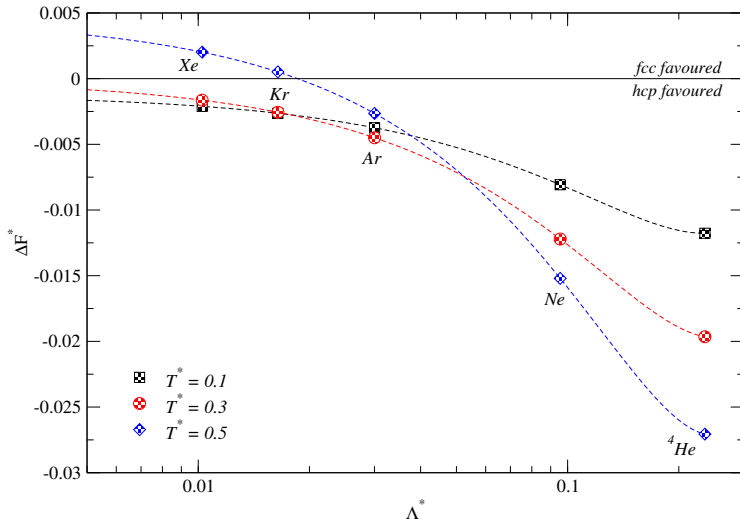
FIG. 14. $\Lambda^*$ values for the noble gases (data points) superimposed on our quantum GSP-corrected $\Delta F^*$ results from Figure 3 (dotted lines), represented here as zero-pressure isotherms at $T^* = 0.1$, 0.3 and 0.5. A log scale is used to show detail near $\Lambda^* = 0$. The $\sigma$ and $\varepsilon$ parameters needed to calculate $\Lambda^*$ were taken from ref. 57 for helium and ref. 11 for Ne, Ar, Kr and Xe.

Keeping in mind that QHLD is a perturbation method, the question remains as to whether any crystal structure *is* stable for $\Lambda \gtrsim 0.3$ at such pressures. In this work we have only considered the hcp and fcc phases, which are the only two phases known to be stable in the classical LJ solid. Of course, there is the prospect that phases other than hcp and fcc are stable at certain temperatures and low pressures for the quantum LJ solid.

## VI. CONCLUSION

Through a combination of PIMD simulations and lattice dynamics calculations, the inclusion of nuclear quantum effects in the LJ solid has been shown to stabilize the fcc phase at low temperature and the hcp phase at high temperature. In addition, the quantum effects on the phase behaviour of the quantum LJ solid in PIMD is relatively insensitive to the truncation scheme or cutoff length used, which makes it somewhat easier to draw definitive conclusions than their classical counterparts - despite the increased computational cost. We also offer an explanation for the experimentally observed phase behaviour of the noble gas solids. Helium, which is highly quantum, has a sufficiently large de Boer parameter that it falls squarely in the quantum-favoured hcp region. Thus the contrast between hcp helium

27

and fcc structures for the other noble gases solids is purely due to quantum effects.

## ACKNOWLEDGMENTS

## SUPPLEMENTARY MATERIAL

See supplementary material for the methodology underpinning both PIMD and QHLD calculations, a discussion of the convergence of PIMD and an examination of exchange effects in the quantum LJ solid.

## DATA AVAILABILITY

The data that support the findings of this study are openly available from Edinburgh DataShare[58] at https://doi.org/10.7488/ds/2846.

## REFERENCES

[1] J. E. Jones, "On the determination of molecular fields. —II. From the equation of state of a gas," Proceedings of the Royal Society A **106**, 463–477 (1924).

[2] T. Kihara and S. Koba, "Crystal structures and intermolecular forces of rare gases," Journal of the Physical Society of Japan **7**, 348–354 (1952).

[3] A. Jackson, A. Bruce, and G. Ackland, "Lattice-switch monte carlo method: Application to soft potentials," Physical Review E **65**, 036710 (2002).

[4] A. Travesset, "Phase diagram of power law and lennard-jones systems: Crystal phases," The Journal of Chemical Physics **141**, 164501 (2014).

[5] H. Adidharma and S. P. Tan, "Accurate monte carlo simulations on fcc and hcp lennard-jones solids at very low temperatures and high reduced densities up to 1.30," The Journal of Chemical Physics **145**, 014503 (2016).

[6]C. Calero, C. Knorowski, and A. Travesset, "Determination of anharmonic free energy contributions: Low temperature phases of the lennard-jones system," The Journal of Chemical Physics **144**, 124102 (2016).

[7]P. Schwerdtfeger, N. Gaston, R. P. Krawczyk, R. Tonner, and G. E. Moyano, "Extension of the lennard-jones potential: Theoretical investigations into rare-gas clusters and crystal lattices of he, ne, ar, and kr using many-body interaction expansions," Phys. Rev. B **73**, 064112 (2006).

[8]C. H. Loach and G. J. Ackland, "Stacking characteristics of close packed materials," Physical Review Letters **119**, 205701 (2017).

[9]L. B. Pártay, C. Ortner, A. P. Bartók, C. J. Pickard, and G. Csányi, "Polytypism in the ground state structure of the lennard-jonesium," Physical Chemistry Chemical Physics **19**, 19369–19376 (2017).

[10]J.-P. Hansen and L. Verlet, "Phase transitions of the lennard-jones system," Physical Review **184**, 151–161 (1969).

[11]G. Rutkai, M. Thol, R. Span, and J. Vrabec, "How well does the lennard-jones potential represent the thermodynamic properties of noble gases?" Molecular Physics **115**, 1104–1121 (2017).

[12]B. Saager and J. Fischer, "Predictive power of effective intermolecular pair potentials: Md simulation results for methane up to 1000 mpa," Fluid Phase Equilibria **57**, 35 – 46 (1990).

[13]L. H. Nosanow, L. J. Parish, and F. J. Pinski, "Zero-temperature properties of matter and the quantum theorem of corresponding states: The liquid-to-crystal phase transition for fermi and bose systems," Phys. Rev. B **11**, 191–204 (1975).

[14]C. P. Herrero and R. Ramírez, "Rare-gas solids under pressure: A path-integral monte carlo simulation," Physical Review B **71**, 174111 (2005).

[15]R. J. Hardy, D. J. Lacks, and R. C. Shukla, "Quantum corrections to the simulated properties of solids," Physical Review B **57**, 833–838 (1998).

[16]R. G. Della Valle and E. Venuti, "Quasiharmonic lattice-dynamics and molecular-dynamics calculations for the lennard-jones solids," Physical Review B **58**, 206–212 (1998).

[17]C. Chakravarty, "Path integral simulations of quantum lennard-jones solids," The Journal of Chemical Physics **116**, 8938 (2002).

[18]C. Chakravarty, "Energy landscapes of quantum lennard-jones solids," The Journal of Physical Chemistry A **115**, 7028–7033 (2011).

[19] A. Cuccoli, A. Macchi, V. Tognetti, and R. Vaia, "Monte carlo computations of the quantum kinetic energy of rare-gas solids," Phys. Rev. B **47**, 14923–14931 (1993).

[20] C. P. Herrero, "Isotopic effect in the lattice parameter of rare-gas solids," Journal of Physics: Condensed Matter **15**, 475–488 (2003).

[21] R. Ramírez and C. P. Herrero, "Anharmonic phonon energies in rare-gas solids derived by path-integral simulations," Phys. Rev. B **72**, 024303 (2005).

[22] L. H. Nosanow, "Generalized phase diagram and critical behavior for quantum systems," Journal of low temperature physics **26**, 613–626 (1977).

[23] C. Chakravarty, "Isothermal-isobaric ensemble simulations of melting in quantum solids," Phys. Rev. B **59**, 3590–3598 (1999).

[24] B. Fultz, "Vibrational thermodynamics of materials," Progress in Materials Science **55**, 247 – 352 (2010).

[25] K. Rościszewski and B. Paulus, "Influence of three-body forces and anharmonic effects on the zero-point energy of rare-gas crystals," Phys. Rev. B **66**, 092102 (2002).

[26] C. Cazorla and J. Boronat, "Simulation and understanding of atomic and molecular quantum crystals," Reviews of Modern Physics **89**, 035003 (2017).

[27] D. M. Ceperley, "Path integrals in the theory of condensed helium," Reviews of Modern Physics **67**, 279–355 (1995).

[28] C. P. Herrero and R. Ramírez, "Path-integral simulation of solids," Journal of Physics: Condensed Matter **26**, 233201 (2014).

[29] A review of experimental findings regarding the low pressure phase behaviour of the heavy noble-gas solids can be found in ref. 37, pp. 159–163.

[30] C. Cazorla and J. Boronat, "Atomic kinetic energy, momentum distribution, and structure of solid neon at zero temperature," Phys. Rev. B **77**, 024310 (2008).

[31] F. Cinti, T. Macrì, W. Lechner, G. Pupillo, and T. Pohl, "Defect-induced supersolidity with soft-core bosons," Nature Communications **5**, 3235 (2014).

[32] J. D. Boer, "Quantum effects and exchange effects on the thermodynamic properties of liquid helium," in *Progress in Low Temperature Physics*, Vol. 2, edited by C. Gorter (Elsevier, 1957) pp. 1 – 58.

[33] D. Frenkel and B. Smit, *Understanding Molecular Simulation*, 2nd ed. (Academic Press, San Diego, 2002).

[34]J. E. Jones and A. E. Ingham, "On the calculation of certain crystal potential constants, and on the cubic crystal of least potential energy," Proceedings of the Royal Society A **107**, 636–653 (1925).

[35]T. H. K. Barron and C. Domb, "On the cubic and hexagonal close-packed lattices," Proceedings of the Royal Society A **227**, 447–465 (1955).

[36]F. H. Stillinger, "Lattice sums and their phase diagram implications for the classical lennard-jones model," The Journal of Chemical Physics **115**, 5208–5212 (2001).

[37]A. N. Jackson, *Structural Phase Behaviour Via Monte Carlo Techniques*, Ph.D. thesis, University of Edinburgh (2001).

[38]D. Frenkel and A. J. C. Ladd, "New monte carlo method to compute the free energy of arbitrary solids. application to the fcc and hcp phases of hard spheres." The Journal of Chemical Physics **81**, 3188 (1984).

[39]C. Vega, E. Sanz, J. L. F. Abascal, and E. G. Noya, "Determination of phase diagrams via computer simulation: methodology and applications to water, electrolytes and proteins," Journal of Physics: Condensed Matter **20**, 153101 (2008).

[40]J. L. Aragones, C. Valeriani, and C. Vega, "Note: Free energy calculations for atomic solids through the einstein crystal/molecule methodology using gromacs and lammps," The Journal of Chemical Physics **137**, 146101 (2012).

[41]S. Plimpton, "Fast parallel algorithms for short-range molecular dynamics," Journal of Computational Physics **117**, 1–19 (1995).

[42]V. Kapil, M. Rossi, O. Marsalek, R. Petraglia, Y. Litman, T. Spura, B. Cheng, A. Cuzzocrea, R. H. Meißner, D. M. Wilkins, B. A. Helfrecht, P. Juda, S. P. Bienvenue, W. Fang, J. Kessler, I. Poltavsky, S. Vandenbrande, J. Wieme, C. Corminboeuf, T. D. Kühne, D. E. Manolopoulos, T. E. Markland, J. O. Richardson, A. Tkatchenko, G. A. Tribello, V. V. Speybroeck, and M. Ceriotti, "i-pi 2.0: A universal force engine for advanced molecular simulations," Computer Physics Communications **236**, 214 – 223 (2019).

[43]M. Ceriotti, M. Parrinello, T. E. Markland, and D. E. Manolopoulos, "Efficient stochastic thermostatting of path integral molecular dynamics," The Journal of Chemical Physics **133**, 124104 (2010).

[44]J. R. Morris and X. Song, "The melting lines of model systems calculated from coexistence simulations," The Journal of Chemical Physics **116**, 9352–9358 (2002).

[45] E. A. Mastny and J. J. de Pablo, "Melting line of the lennard-jones system, infinite size, and full potential," The Journal of Chemical Physics **127**, 104504 (2007).

[46] P. Esbjørn, E. Jensen, W. Kristensen, J. Martin, and L. Pedersen, "Entropy of fcc and hcp lattices: Comparison of h theorem method with vibrational analysis," Journal of Computational Physics **12**, 289 – 307 (1973).

[47] P. G. Bolhuis, D. Frenkel, S.-C. Mau, and D. A. Huse, "Entropy difference between crystal phases," Nature **388**, 235–236 (1997).

[48] S.-C. Mau and D. A. Huse, "Stacking entropy of hard-sphere crystals," Physical Review E **59**, 4396–4401 (1999).

[49] A. Bruce, A. Jackson, G. Ackland, and N. Wilding, "Lattice-switch monte carlo method," Physical Review E **61**, 906 (2000).

[50] V. Elser, "Phonon contribution to the entropy of hard-sphere crystals," Physical Review E **89**, 052404 (2014).

[51] J. D. Gale and A. L. Rohl, "The General Utility Lattice Program (GULP)," Molecular Simulation **29**, 291–341 (2003).

[52] G. L. Pollack, "The solid state of rare gases," Reviews of Modern Physics **36**, 748–791 (1964).

[53] J. M. McMahon, M. A. Morales, C. Pierleoni, and D. M. Ceperley, "The properties of hydrogen and helium under extreme conditions," Reviews of Modern Physics **84**, 1607–1653 (2012).

[54] J. Cuthbert and J. W. Linnett, "The crystal structure of the group 0 elements," Transactions of the Faraday Society **54**, 617–622 (1958).

[55] K. F. Niebel, J. A. Venables, and C. A. Coulson, "An explanation of the crystal structure of the rare gas solids," Proceedings of the Royal Society A **336**, 365–377 (1974).

[56] B. Borden and C. Radin, "The crystal structure of the noble gases," The Journal of Chemical Physics **75**, 2012–2013 (1981).

[57] R. G. Gordon and Y. S. Kim, "Theory for the forces between closed-shell atoms and molecules," The Journal of Chemical Physics **56**, 3122–3133 (1972).

[58] H. Wiebe, T. Underwood, and G. J. Ackland, "Phase behaviour of the quantum lennard-jones solid, [dataset]," University of Edinburgh. School of Physics & Astronomy. https://doi.org/10.7488/ds/2846 (2020).